



**Environmental
Science**
Nano

**Photo-production of Reactive Oxygen Species and
Degradation of Dissolved Organic Matter by Hematite
Nanoplates Functionalized by Adsorbed Oxalate**

Journal:	<i>Environmental Science: Nano</i>
Manuscript ID	EN-ART-04-2020-000365.R1
Article Type:	Paper

SCHOLARONE™
Manuscripts

Environmental Significance Statement

Natural and anthropogenic nanomaterials are ubiquitous in aqueous environments and appear intimately linked with biogeochemical cycles on earth. However, the photocatalytic interactions between organic-coated iron oxide nanoparticles and dissolved organic matter (DOM), an interaction that may strongly couple the cycling of iron and carbon in the euphotic zone of natural waters remains elusive. Here we report a systematic study of the indirect photodegradation of two water-extractable chromophoric DOM compounds from Midwest agricultural soils by hematite nanoplates functionalized by adsorbed oxalate. The findings suggest that this indirect DOM photodegradation pathway is significant in aquatic systems where these components pervade, adding a controlling process to the total DOM pool in euphotic zones and thereby impacting the global carbon cycle.

Photo-production of Reactive Oxygen Species and Degradation of Dissolved Organic Matter by Hematite Nanoplates Functionalized by Adsorbed Oxalate

Xiaopeng Huang,^{,†} Qian Zhao,[‡] Robert P. Young,[‡] Xin Zhang,[†] Eric D. Walter,[‡] Ying Chen,[‡] Elias Nakouzi,[†] Sandra D. Taylor,[†] John S. Loring,[†] Zheming Wang,[†] Kirsten S. Hofmockel[‡] and Kevin M. Rosso^{*,†}*

[†]Physical and Computational Sciences Directorate, Pacific Northwest National Laboratory,
Richland, Washington 99352, United States

[‡]Environmental Molecular Sciences Laboratory, Pacific Northwest National Laboratory, Richland,
Washington 99352, United States

*To whom correspondence should be addressed.

(K.M.R) kevin.rosso@pnnl.gov, +1-509-371-6357;

(X.H.) xiaopeng.huang@pnnl.gov, +1-509-375-6719.

Abstract. The geochemical cycling of iron and carbon can couple in unique ways in the euphotic zone of aquatic systems. For example, the prevalence of hematite nanoparticles and low molecular weight organics that can functionalize their surfaces, such as oxalate, creates a solar- photoactive interfacial system capable of generating reactive oxygen species (ROS) that degrade natural organic matter. Here we report a systematic study of this pathway and its efficiency to mineralize model chromophoric dissolved organic matter (DOM) compounds into CO₂ under mildly acidic conditions. When illuminated, synthetic hematite nanoplates coated with adsorbed oxalate undergo ligand-to-metal charge transfer yielding Fe(II) via photoreductive dissolution, while oxalate decomposes into the carboxyl anion radical as detected by electron paramagnetic spectroscopy using selective spin trap compounds. This important radical quickly reduces molecular oxygen into hydrogen peroxide, which initiates the canonical Fenton reactions that yield hydroxyl radical via Fe(II)/Fe(III) valence cycling. Production of hydroxyl radical in this photocatalytic system is shown to efficiently degrade the pseudo-DOM chromophore RhB, as well as two natural water-extractable chromophoric DOM compounds from agricultural soils, characterized in molecular detail using Fourier transform ion cyclotron resonance mass spectrometry, infrared fluorescence and nuclear magnetic resonance spectroscopies. The study highlights the photocatalytic interactions that can occur between common iron oxide nanoparticles, low molecular weight dicarboxylic acids, and dissolved organic matter that can couple their steady-state fluxes in the euphotic zone, pointing to the importance of light-induced ROS generation as a key mechanism.

1. INTRODUCTION

Natural and anthropogenic nanomaterials are ubiquitous in aquatic environments and thus can exert an important influence on various biogeochemical cycles on earth.^{1, 2} For example, in the euphotic

1 zone, hematite ($\alpha\text{-Fe}_2\text{O}_3$) nanoparticles^{3, 4} play a central role in the iron biogeochemical cycling that
2
3 impacts other elemental cycles,^{5, 6} nitrogen fixation^{7, 8}, photosynthesis,⁹ as well as elimination of
4
5 persistent organic micropollutant in nature¹⁰⁻¹². The photochemical dissolution of iron oxides is
6
7 regarded as an indispensable function in sustaining the bioavailability of iron,^{13, 14} a particularly
8
9 critical factor in controlling phytoplankton growth in the ocean.^{15, 16}
10
11
12

13
14 Turnover of natural dissolved organic matter (DOM) in the euphotic zone is also strongly
15
16 coupled to the interaction of light with hematite nanoparticles, though the specific reaction pathways
17
18 by which this occurs remain poorly understood. Derived from biological sources,¹⁷ DOM
19
20 encompasses millions of organic molecules that comprise a critical component of the global carbon
21
22 cycle.¹⁸ DOM often contains light-absorbing chromophore groups,¹⁹ which give rise to its color as
23
24 well as its propensity to be directly photodegraded. However, common low molecular weight
25
26 (LMW) carboxylic organic substances (e.g., oxalic acid) that bind to iron oxide surfaces can
27
28 photocatalyze the production of reactive oxygen species (ROS) through interfacial electron transfer
29
30 and valence cycling of iron sites at the interface. The mechanism involved was well applied in
31
32 remediation strategies of organic pollutants. For instance, Lan et al investigated the
33
34 photodegradation of pentachlorophenol in the presence of iron oxides and oxalate under UV
35
36 illumination.^{20, 21} Similarly, Huang et al. investigated the photodegradation of norfloxacin in the
37
38 presence of various iron oxides and oxalate under UV illumination.²² However, all of them are
39
40 focused on simulated remediation/environmental engineering applications of toxic organic chemicals
41
42 based on laboratory conditions, the generation of involved ROS were not directly confirmed, and the
43
44 intrinsic mechanism is ambiguous since the structures of these iron oxides were not as thoroughly
45
46 characterized. To constrain the mechanism in detail, a highly precise, controlled iron oxide material,
47
48 such as the hematite nanoplates in the present study, are preferable to the irregular iron oxide
49
50
51
52
53
54
55
56
57
58
59
60

1 particles used previously. What's more, cycling processes of DOM from real soils in contact with
2
3 hematite and oxalate has long been overlooked due to the complicated character of natural DOM
4
5 samples. As the electrophilic nature of ROS leads to facile reaction with the electron-rich functional
6
7 groups in DOM, the consequent background ROS flux could thus also comprise a photodegradation
8
9 pathway, albeit indirectly via photosensitization of hematite nanoparticles by adsorbed oxalate.
10
11
12

13
14 In this regard, it is well documented that ligand to metal charge transfer (LMCT) in the
15
16 photolysis of iron-oxalate complexes can generate bioavailable ferrous iron and environmentally
17
18 persistent ROS, such as singlet oxygen ($^1\text{O}_2$), hydroxyl radicals ($\cdot\text{OH}$), superoxide anion radicals ($\cdot\text{O}_2^-$),
19
20 and hydrogen peroxide (H_2O_2).^{23, 24} Bleaching of naturally occurring organics by these ROS
21
22 then produces identifiable LMW organics and mineralized inorganic species (e.g., CO_2), according
23
24 to the general scheme:
25
26
27



30
31
32
33
34 In this regard, it is noteworthy that the LMW products include the prospect of regeneration of
35
36 oxalate,²⁵ which could help maintain the concentration of this photosensitizer and propagate the
37
38 indirect photodegradation process. In addition to the euphotic zone, such processes have also been
39
40 documented for atmospheric aerosol particles.^{24, 26, 27}
41
42
43
44

45
46 Photo-induced iron redox cycling with consequent ROS production has been shown to enhance
47
48 the bleachability of terrestrially derived DOM.²⁸ Likewise, photoproduction of hydroxyl radicals can
49
50 steadily bleach DOM in open-ocean surface water, impacting organics and biota in deeper
51
52 seawater.²⁹ Prior work is thus strongly suggestive that the indirect photodegradation of DOM by
53
54 environmentally persistent ROS may significantly impact the total DOM pool and the global carbon
55
56 cycle. However, the LMCT process for iron-oxalate complexes under illumination, particularly when
57
58
59
60

1 involving hematite nanoparticles, and the reactivity of DOM with the resulting ROS has yet to be
2
3 specifically examined.
4

5
6 Here we do so, using a well-defined model system of synthetic hematite nanoparticles,
7
8 functionalized by adsorbed oxalate, under mildly acidic conditions, with illumination designed to
9
10 mimic the frequency range and irradiance of solar light, and using various representations of DOM.
11
12 The adsorption of oxalate onto size and morphologically controlled hematite nanoplates, and their
13
14 subsequent photodissolution under illumination were systematically investigated with Fourier
15
16 transform infrared (FTIR) spectroscopy, aqueous analytical dissolution kinetics, transmission
17
18 electron microscopy (TEM), and scanning transmission electron microscopy (STEM). Electron
19
20 paramagnetic resonance (EPR) spectroscopy was then used to detect and characterize associated
21
22 ROS during illumination, the reactivity of which was first evaluated using the dye rhodamine B
23
24 (RhB) as a proxy for the chromophoric component of DOM. Finally, degradation of naturally
25
26 chromophoric DOM was examined using DOM extracted from two agricultural soils, with
27
28 generalized molecular characterization using ^1H nuclear magnetic resonance (NMR) spectroscopy,
29
30 Fourier transform ion cyclotron resonance mass spectrometry (FTICR-MS), and FTIR spectroscopy.
31
32 The collective findings establish the efficacy of this indirect DOM photodegradation pathway,
33
34 shedding light on important ROS species and the mechanism. As a major result, the prospect of this
35
36 photochemical cycle mediated by hematite nanoparticles impacting the dynamics of natural organic
37
38 matter in the euphotic zone is suggested.
39
40
41
42
43
44
45
46
47
48
49
50
51
52

53 **2. Experimental Section**

54
55 **2.1 Materials.** 5-(diethylphosphono)-5-methyl-1-pyrroline N-oxide (DEPMPO),
56
57 5,5-Dimethyl-1-Pyrroline N-oxide (DMPO), and other reagents were obtained from Sigma-Aldrich.
58
59
60

1 Text S1 in the Supporting Information provides further details regarding materials used in this study.
2

3 **2.2 Synthesis.** The synthesis method used for the hematite nanoplates is described in our previous
4 work (see Text S2 in the Supporting Information),³⁰ and the same material has been used in prior
5 reactivity studies.³¹
6
7
8

9
10 **2.3 Characterization.** The morphology and crystallinity of the hematite sample were investigated
11 by high-resolution transmission electron microscopy (HRTEM) and high-angle annular dark-field
12 (HADDF) scanning transmission electron microscope (STEM). Further details regarding the
13 analyses of defects of hematite nanoplates are described in Text S3 the Supporting Information.
14
15
16
17
18
19

20 **2.4 Experimental pH.** Unless otherwise stated, all experiments were performed at the mildly acidic
21 pH of 4, a value chosen to optimize experimentally accessible mechanistic insight. For example, this
22 value enabled real-time examination of oxalate-assisted hematite photodissolution rates and
23 consequent surface dissolution features. It also optimized ROS generation by Fenton reactions, while
24 preserving the ability to isolate by EPR specific radical species using pH-sensitive scavenger
25 molecules such as DEPMPO and DMPO.
26
27
28
29
30
31
32
33
34
35

36 **2.5 Analytical Methods.** The sophisticated spectroscopic methods including the measurement of
37 oxalate coordination on hematite by infrared spectra, H₂O₂ measurement by UV-vis, and
38 fluorescence emission spectra are described in detail in Text S4 in the Supporting Information.
39
40
41
42
43
44

45 **2.6 EPR Spectroscopy.** All EPR measurements were performed on Bruker ELEXSYS E580
46 spectrometer equipped with an SHQE resonator with an optical access port for *in situ* illumination,
47 which are described in detail in Text S5 in the Supporting Information.
48
49
50
51

52 **2.7 Natural DOM Extraction.** The methods of dissolved organic matter extracted from Wisconsin
53 soil (DOM_{WS}) and Michigan soil (DOM_{MS}) are described in detail in Text S6 in the Supporting
54 Information.
55
56
57
58
59
60

1 **2.8 FTICR MS Data Acquisition and Data Analysis.** For ultrahigh resolution characterization of
2
3 dissolved organic matter, the samples extracted from soil were analyzed using a 12 Tesla FTICR
4
5 mass spectrometer (Bruker-SolariX) that uses an electrospray ionization (ESI) source to generate
6
7 negatively charged molecular ions. The methods are described in detail in Text S7 of the Supporting
8
9 Information.
10
11

12
13 **2.9 Nuclear Magnetic Resonance (NMR) Spectroscopy.** Measurements were conducted using a
14
15 Bruker Avance III spectrometer operating at a field strength of 17.6 T (^1H ν_0 of 750.24 MHz) and
16
17 equipped with a 5mm Bruker TCI/CP HCN (inverse) cryoprobe. 1D ^1H NMR spectra were acquired
18
19 on samples in 100% D_2O with the W5-WATERGATE pulse program ('zggpw5')³² that included 128
20
21 transients acquired with a 1.4 s acquisition time (16k TD points, 16 ppm spectral width), and 45 s
22
23 relaxation delay. Post-acquisition processing included zero-filling to 32k points and multiplication
24
25 by a decaying exponential function (line broadening of 5 Hz). Additional experimental details are
26
27 provided in Text S8 of the Supporting Information.
28
29
30
31
32
33

34 **2.10 Photodegradation Experiments.** The photodegradation experiments were set up according to
35
36 our previous study,³⁰ and are described in detail in Text S9 in the Supporting Information.
37
38
39
40
41

42 **3. Results and Discussion**

43
44 **3.1 Hematite Nanoplates.** TEM images of the as-prepared hematite particles showed the desired
45
46 hexagonal nanoplate morphology in which the length and thickness of the nanoplates were about
47
48 93.5 and 13.1 nm, respectively (Fig. 1A). HRTEM indicated that nanoplates were highly crystalline;
49
50 three sets of distinguishable lattice fringes of 0.25 nm agreed with (110), (-210), (-120) planes in the
51
52 fast Fourier transformation (FFT) pattern (Fig. 2B). Hence, nanoplates were enclosed with basal
53
54 (001) and edge (012) facets. STEM images displayed that the diameter and thickness were the same
55
56
57
58
59
60

as that interpreted from TEM images (Fig. 1C). Zoomed in STEM imaging could resolve individual nanoplates (Fig. 1D), which displayed characteristic spectral features in electron energy loss spectral mapping at the Fe L-edge (Fig. 1E), Fe K-edge (Fig. 1F), and O K-edge (Fig. 1G).

3.2 Photodissolution of Hematite Nanoplates. ATR-FTIR spectroscopy was used to characterize how oxalate coordinates at the hematite surface as a surface complex.



Binding can occur either as predominantly outer-sphere or inner-sphere complexes, or a combination (see Fig. 2B).³³ In outer-sphere complexes, water molecules remain between the hematite surface and oxalate. A model for outer-sphere oxalate is that of the unprotonated oxalate anion, which has bands at 1568 and 1307 cm^{-1} , corresponding to the degenerated asymmetric stretching of C-O ($\nu^{\text{as}}_{\text{C-O}}$) and symmetric stretching of C-O ($\nu^{\text{s}}_{\text{C-O}}$), respectively (Fig. 2A).³³ For inner-sphere complexes, oxalate is bound directly to Fe(III) in a bidentate chelating fashion. A model for this type of coordination geometry is the trioxalatoiron(III) anion, which has peaks at 1710, 1683, 1392, and 1267 cm^{-1} attributed to the stretching of C-O ($\nu^{\text{nb}}_{\text{C-O}}$), second harmonic stretching of C-O ($\nu^{\text{nb}}_{\text{C-O}}$), coupled stretching of C-O and C-C ($\nu^{\text{b}}_{\text{C-O+C-C}}$), and coupled stretching of C-O and bending of O-C-O ($\nu^{\text{b}}_{\text{C-O}} + \delta_{\text{O-C-O}}$) (where nb and b represent the oxygen of the carboxylate group not bonded to iron and the oxygen of the carboxylate group bonded to iron, respectively), consistent to our previous study,³³ and Persson and Axe's research.³⁴

For hematite nanoplates after reaction with oxalate at our experimental pH of 4, in the absence of light, four peaks could be identified at 1705, 1687, 1404 and 1249 cm^{-1} , consistent with inner-sphere coordinated oxalate. There was no evidence for intensity at around 1568 and 1307 cm^{-1} , indicating that the outer-sphere iron-oxalate complexes was negligible. The same four peaks were observed under simulated solar light illumination, indicating the predominantly inner-sphere surface

1 complex formation on hematite. However, although the frequencies were the same, close
2
3 examination showed a slight intensity decrease of all four peaks compared to spectra collected in the
4
5 absence of illumination. For instance, the intensity decreased 14.54% at 1687 cm^{-1} under
6
7 illumination. This suggested that surface iron-oxalato complexes were decomposing under
8
9 illumination, generally consistent with prior studies,^{20, 35} reducing the amount of oxalate adsorbed on
10
11 the hematite surfaces.
12
13
14
15

16 In addition, the formation of such inner sphere complexes has been regarded as the hematite
17
18 surface activation process – the primary step for the dissolution of hematite.^{36, 37} This surface
19
20 activation could be interpreted in terms of Lewis acid-base theory. The surface of hematite can be
21
22 regarded as a Lewis acid under mildly acidic conditions at pH 4, the exposed iron cations on the
23
24 hematite surface would be sufficiently bound by the Lewis base which are the negatively charged
25
26 oxalate species. The surface complexation is hence primed for reductive dissolution. For instance,
27
28 the formation of ascorbic acid inner-sphere bidentate and monodentate mononuclear complexes on
29
30 the hematite (001) and (012) facets, respectively, which was confirmed by the combination of IR
31
32 spectra and theoretical calculations, showed different reductive dissolution behavior.¹⁴ The bidentate
33
34 complexes on hematite (001) facets facilitated reductive dissolution more, in comparison with the
35
36 monodentate ones on the (012) facets.¹⁴ Hematite (001) and (012) facets generally possess iron sites
37
38 of different coordination,^{4, 14} accounting for the facet-dependent adsorption of ascorbic acid.
39
40 However, for the nanoplates in the current study the proportion of basal (001) plane exposure is
41
42 roughly seven times larger than the edge (012) facets.³⁰ Under this circumstance, to observe the
43
44 spectral contribution from the (012) facets in the current experimental setup would be difficult. In
45
46 future work, comparison to particles bearing dominantly (012) facets could be useful to further
47
48 evaluate facet-dependent adsorption mechanisms. Therefore, here we consider primarily the
49
50
51
52
53
54
55
56
57
58
59
60

1 bidentate inner sphere complexes of oxalate formed (001) exposed facets as primarily responsible
2
3 for observed dissolution.
4

5
6 Given the expectation of photocatalyzed decomposition of adsorbed oxalate by LMCT to surface
7
8 Fe(III) sites yielding Fe(II), we examined the dissolution kinetics of the nanoplates with and without
9 illumination (Fig. 2C). For reference, the concentration of dissolved iron without oxalate at pH 4,
10
11 irrespective of illumination, remained under the detection limit of the 1, 10-phenanthroline
12
13 colorimetric method,³⁸ thus proton-assisted dissolution of hematite was safely negligible in all
14
15 experiments. In the absence of light, the total concentration of aqueous Fe, and its Fe(II) fraction
16
17 both increased to 8.76×10^{-5} and 1.94×10^{-5} mol/L respectively after 7 h. Fe(III) was predominantly
18
19 generated compared to Fe(II) (22.15%), most likely resulting from ligand-promoted dissolution of
20
21 the hematite nanoplates. The non-negligible amount of Fe(II) production indicated that mild
22
23 reductive dissolution by spontaneous oxalate decomposition was operable under our conditions.
24
25 However, under light illumination, over the same time period the concentrations of total dissolved
26
27 iron and Fe(II) reached 3.99×10^{-4} and 1.72×10^{-4} mol/L, respectively. In this case, the much larger
28
29 Fe(II) fraction (43.11%) indicated substantial photocatalyzed LMCT and photoreductive dissolution
30
31 occurred. In addition, the 8.87x increase in Fe(II) production was accompanied by a 2.84x increase
32
33 in Fe(III) production, suggesting that light enhanced both reductive and ligand-promoted dissolution
34
35 kinetics. In addition, Fe(II) was not observed with hematite alone under illumination because of the
36
37 relative inefficiency of this process due to the ultrafast electron-hole recombination time (1 ps) and
38
39 short hole diffusion length (2-4 nm) of hematite.^{39, 40} This confirms that the direct photodissolution
40
41 of the hematite nanoplates directly by band gap excitation (2.09 eV for hematite nanoplates in our
42
43 previous study)³⁰ should be negligible compared to the observed photodissolution by LMCT.
44
45
46
47
48
49
50
51
52
53
54
55
56

57
58 Previous research demonstrated that Fe(II) was slowly released into the solution at the beginning
59
60

1 of the induction period after the primary surface activation period and during the dissolution of
2
3 hematite by oxalate.^{36, 37} As the reaction proceeds, accumulation of a sufficient amount of Fe(II) in
4
5 the solution, which leads to formation of iron(II)-oxalato complexes, can accelerate further
6
7 detachment of Fe(II) from the surface, which is known as the autocatalytic dissolution period.^{35, 36}
8
9 The pseudo-zero-order-rate constant (k) of Fe(II) production in the solution was $0.0027 \text{ mmol L}^{-1} \text{ h}^{-1}$
10
11 for the dissolution of hematite by oxalate in the dark, due to an insufficient amount of produced
12
13 Fe(II) in the induction period during the whole process (Fig. 2C). In the hematite dissolution by
14
15 oxalate under light, Fe(II) was slowly released at a k of $0.0121 \text{ mmol L}^{-1} \text{ h}^{-1}$ in the induction period
16
17 within 3 hours (Fig. 2C). After 3 hours, a sufficient accumulation of Fe(II) in the solution increased
18
19 the Fe(II) production autocatalytically and, as a result, the corresponding k reached $0.0348 \text{ mmol L}^{-1}$
20
21 h^{-1} , 2.88 times larger than its induction rate constant.
22
23
24
25
26
27
28
29

30 In addition, in the presence of oxalate under illumination, the density of the surface adsorbed
31
32 Fe(II) on hematite extracted by HCl methods^{11, 14} was measured to be $1.16 \times 10^{-6} \text{ mol/m}^2$ which was
33
34 approximately 4 times larger than the controlled dark reaction ($2.83 \times 10^{-7} \text{ mol/m}^2$) (inserted in Fig.
35
36 2C), suggesting the occurrence of LMCT process on hematite surface.
37
38
39

40 To examine facet-specific aspects of the photoreductive dissolution of oxalate-coated hematite
41
42 nanoplates, we collected and washed the solids after reaction and then used TEM and
43
44 HADDF-STEM to examine the reacted particle morphology in detail (Fig. 3; Table S1 in the
45
46 Supporting Information). Although major features remained unchanged, defects consistent with
47
48 dissolution features were evident at fine scales. For example, compared to the as-synthesized
49
50 material (Fig. 3A), after photoreaction quantitative TEM image analysis of (001) surfaces indicated
51
52 that 2.44% of the area was attributable to defects of 0.1434 nm^2 average size, yielding a density of
53
54 $2.14 \times 10^{-4} \text{ defects/nm}^2$ (Figs. 3B, C). HADDF-STEM was used to characterize these (001) defects
55
56
57
58
59
60

1 independently, and similar results were obtained. The defect area, average defect size and defect
2
3 densities, which were found 0.40%, 0.0225 nm² and 0.50×10⁻⁴ defects/nm², respectively on
4
5 unreacted material (Figs. 3D, E), increased to 2.55%, 0.0608 nm², and 2.31×10⁻⁴ defects/nm²,
6
7 respectively. The 2.70 times increase of the defect size on photoreacted materials as compared to
8
9 that of the unreacted counterpart offered clear evidence of (001) photodissolution.
10
11
12

13
14 The (012) edge surfaces were likewise examined after photoreaction. Defect areas, average
15
16 defect size and defect densities were respectively analyzed to be 0.17%, 0.0236 nm² and 0.021×10⁻⁴
17
18 defects/nm², slightly lower than that on unreacted (012) surfaces (0.19%, 0.0382 nm² and 0.018×10⁻⁴
19
20 defects/nm², respectively). From this we conclude that these small differences are within the
21
22 statistical sampling error of the image analytical method, and that photodissolution of (012) facets
23
24 was likely much less favorable than that on basal (001) surfaces of the nanoplates.
25
26
27
28

29 **3.3 ROS Generation Investigated by EPR.** EPR spectroscopy with selective radical scavenger
30
31 compounds was then employed to investigate the associated ROS and carbon radical generation in
32
33 the suspensions. Figure 4A shows typical DEPMPO-trapped EPR signal changes in aqueous
34
35 solutions as hematite and oxalate reacted under illumination. DEPMPO is a sensitive trap for
36
37 hydroxyl radicals, as well as for various carbon-based radicals. As expected, no signal was detected
38
39 in the absence of illumination (Fig. 4A) because free radicals were not produced by hematite and
40
41 oxalate contact alone, indicating a negligible role of the dark reaction. Furthermore, with light
42
43 illumination, neither hematite nor oxalate alone produced ROS (Fig. 4A), reinforcing that the direct
44
45 photodegradation effect of hematite from band gap excitation or oxalate was negligible.
46
47
48
49
50
51

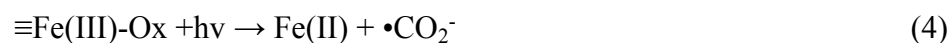
52
53 However, for hematite with oxalate under illumination, multiple peaks were produced in the
54
55 EPR signal, which we quantified as a function of reaction time. Using DEPMPO, we were able to
56
57 assign the peaks according to standard spectra for various species that this molecule is capable of
58
59
60

trapping. For example, the twelve strong straight lines with roughly the same intensity could be assigned to DEPMPO adducts with carboxyl anion radicals (DEPMPO-•CO₂⁻) (Fig. 4B, top). This distinction was enabled in part by test measurements in deoxygenated conditions, in which only the carboxyl anion radical appeared (Fig. 4B, middle), and in which its hyperfine coupling constants of $a_P = 46.3$ G, $a_N = 14.4$ G and $a_H = 21.3$ G were fully consistent with previous studies.⁴¹ Hence, in oxygenated conditions the eight weaker straight lines with intensity of 1:2:2:1:1:2:2:1 could be assigned to the DEPMPO adduct with hydroxyl radical (DEPMPO-•OH) ($a_P = 47.0$ G, $a_N = 14.0$ G and $a_H = 13.0$ G),⁴¹ in agreement with a separate control measurement where hydroxyl radicals form from H₂O₂ alone after 10 seconds UV illumination (Fig. 4B, bottom). Because most of the two sets of peaks arising from the two adducts overlapped, we chose the single non-overlapping peaks at 3269.9 and 3273.9 Gauss as representative of DEPMPO-•CO₂⁻ and DEPMPO-•OH adducts, respectively. Early in the photocatalyzed reaction between oxalate and hematite, we found that the intensity of DEPMPO-•CO₂⁻ and DEPMPO-•OH adducts increased rapidly and plateaued at steady state concentrations within a few minutes of illumination (Fig. 4C). To compare the spin traps, DMPO was also used to characterize the generation of radicals under otherwise identical conditions (Fig. 4D). The DMPO-trapped EPR signal was much weaker than the DEPMPO counterpart but still clearly distinguishable. In this case the six main peaks were attributed to DMPO-•CO₂⁻ adduct with hyperfine coupling constantans of $a_N = 15.7$ G and $a_H = 18.8$ G, in agreement with previous literature.⁴² The four weaker straight lines with intensity ratios of 1:2:2:1 were assigned to DMPO-•OH adduct with $a_N = a_H = 14.7$ G.²⁶ Both of the results from DEPMPO and DMPO solidly confirmed that carboxyl anion radicals and hydroxyl radicals were generated.

Additionally, use of a TiOSO₄/H₂SO₄ reagent enabled us to successfully observe the photochemical formation of H₂O₂,⁴³ whose concentration was found to steadily increase over the

entire course of reaction, achieving 2.8×10^{-4} mol/L within 5 h (Fig. 4E). Analogous to the sudden change of Fe(II) in the solution, the concentration of H_2O_2 also changed greatly at about 3 hours, for reasons discussed in detail below.

3.4 Proposed Photocatalytic Reaction Mechanisms. Within the context of generally known mechanisms of heterogeneous Fenton chemistry,²⁰ these EPR-based observations of radical production are sufficient to propose a photocatalytic reaction mechanism dominating this system. The key initial reaction is the production of Fe(II) and $\bullet\text{CO}_2^-$, which occurs by photolysis of iron-oxalato surface complexes via LMCT:^{35, 44}



Production of $\bullet\text{CO}_2^-$, a transient radical species with a very reducing potential ($E^0_{(\text{CO}_2/\bullet\text{CO}_2)} = -1.8$ V vs SHE,^{26, 45, 46}), is rapidly oxidized to stable CO_2 species by dissolved oxygen. This oxygen reduction reaction (ORR), which activates and cleaves the O-O bond, is known to proceed by a proton-coupled electron transfer (PCET) process.⁴⁷ Reduction products of the ORR can entail complete reduction to H_2O through a four proton-coupled four electron transfer process ($\text{O}_2 + 4e^- + 4\text{H}^+ \rightarrow 2\text{H}_2\text{O}$, $E^0 = 1.229$ V vs SHE), or partial reduction to form H_2O_2 through a two proton-coupled two electron transfer process ($\text{O}_2 + 2e^- + 2\text{H}^+ \rightarrow \text{H}_2\text{O}_2$, $E^0 = 0.695$ V vs SHE).⁴⁸ In our system, because significant photoproduction of H_2O_2 was observed, the latter process appears to be active. One can then write an overall reaction as:



That this reaction should be more favorable than oxygen reduction by Fe(II) is evident by its much higher reductive potential ($E^0_{(\text{Fe(III)/Fe(II)})} = 0.77$ V vs SHE). Reactions 4 and 5 are also consistent with previous research showing the formation of H_2O_2 from direct solar photolysis of iron(III)-oxalato complexes.⁴⁹ Notably, ROS generation from the photolysis of combined ferric and oxalate ions was

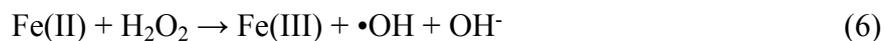
negligible. This was likely due to negligible desorption of the oxalate from the hematite surface indicating a surface-mediated LMCT process for the whole reaction.

More importantly, it was expected that the production of $\bullet\text{CO}_2^-$ was simultaneously accelerated during accelerated Fe(II) release in the autocatalytic dissolution period (equation 4). From equation 4, the molar ratio of produced Fe(II) and $\bullet\text{CO}_2^-$ was quantitatively 1:1, suggesting that the concentration of $\bullet\text{CO}_2^-$ should be equal to Fe(II) during the period when the consumption of these species was neglected. Therefore, the change of $\bullet\text{CO}_2^-$ should be consistent with the change of Fe(II) and, if the production of $\bullet\text{CO}_2^-$ accelerates after 3 hours, the concentration of H_2O_2 would also be expected to accelerate, assuming a constant concentration of dissolved oxygen (equation 5). Indeed, the generation of H_2O_2 was initially slow as $k = 0.0269 \text{ mmol L}^{-1} \text{ h}^{-1}$ during the first 3 hours and greatly accelerated to a higher $k = 0.0435 \text{ mmol L}^{-1} \text{ h}^{-1}$ after 3 hours (Fig. 4E), which was consistent with the abrupt increase of Fe(II) at 3 hours.

With respect to natural environments, it is noteworthy that such a process has also been suggested as one of the most important sources of environmentally persistent H_2O_2 in surface marine waters²⁹ as well as in atmospheric water droplets,⁵⁰ where the key components including LMW organic dicarboxylate substances, iron and oxygen are all abundantly found and they are illuminated by sunlight. Additionally, $\bullet\text{CO}_2^-$ produced *in vivo* in a free radical metabolic pathway has been ascribed as one of the most important reactants generating superoxide anion radicals within bile and urine samples by reduction of molecular oxygen, in this case with a nearly diffusion-controlled rate ($k = 4.2 \times 10^9 \text{ L mol}^{-1} \text{ s}^{-1}$);⁵¹ spontaneous disproportionation of superoxide then enables rapid production of H_2O_2 ($k = 2.3 \times 10^9 \text{ L mol}^{-1} \text{ s}^{-1}$),⁵² the key species leading to $\bullet\text{OH}$ in the Fenton reaction.⁵³

The Fe(II) generated by the photoreductive dissolution of hematite also plays an important role

1 which, given the presence of H₂O₂, initiates the well-known Fenton reactions that produce the
2
3 observed hydroxyl radicals. Summarizing this key aspect, the essential O-O bond heterolysis of
4
5 H₂O₂ triggered by Fe(II) proceeds according to:
6
7



10 This process is maintained by valence cycling of iron - the photoproduction of $\bullet\text{OH}$ with its high
11
12 oxidative potential of $E^0 = +2.7 \text{ eV}$ ⁵⁴ oxidizes Fe(II) to regenerate Fe(III) ($k = 5 \times 10^8 \text{ L mol}^{-1} \text{ s}^{-1}$).⁵⁵
13
14 Noteworthy, the lamp we used essentially provided visible light, and decomposition of H₂O₂ was
15
16 known to be weak under visible light. The observation of a constant increase of H₂O₂ further
17
18 indicated its stability under illumination. Additionally, from the viewpoint of thermodynamics, $\bullet\text{CO}_2$
19
20 would preferentially react with dissolved oxygen instead of H₂O₂. Under these circumstances, $\bullet\text{OH}$
21
22 generation from direct photo-decomposition of H₂O₂ or from $\bullet\text{CO}_2$ was negligible.
23
24
25
26
27
28

29 Having identified the most likely reaction pathways to $\bullet\text{CO}_2^-$ and $\bullet\text{OH}$, we can now address the
30
31 significance of the microscopic observations of preferential dissolution on (001) basal facets relative
32
33 to (012) edge facets. Formation of surface complexes of bound oxalate on hematite nanoplates is
34
35 prerequisite to the photolysis reaction that occurs by LMCT. The donation of electrons to the
36
37 conduction band (CB) of hematite creates a supply of Fe(II) and $\bullet\text{CO}_2^-$. Previous research by our
38
39 group has shown that the extent of iron coordination on the surface plays an important role in the
40
41 reactivity of those sites; three-fold coordinated iron sites (Fe_{3c}) characteristic of hematite (001)
42
43 surfaces tend to be more reactive compared to five-fold coordinated iron cation active sites (Fe_{5c})
44
45 characteristic of hematite (012) surfaces.³⁰ Although for the present system whether this has more to
46
47 do with the increased ability of iron sites on (001) to be complexed by oxalate or their propensity to
48
49 accept electron density by LMCT remains unclear, this nonetheless may explain more facile
50
51 photoreductive dissolution of (001) facets (Fig. 3). This aspect of the importance of individual
52
53
54
55
56
57
58
59
60

1 atomic site types, along with the major important ROS-generating reactions in the photocatalytic
2
3 scheme, are summarized in the conceptual model illustrated in Figure 4F.
4
5

6 **3.5 Coupling to Photodegradation of Chromophoric DOM.** The electrophilic property of
7
8 hydroxyl radicals allows fast destruction of the electron-rich functional groups that endow
9
10 unsaturated bonds and low steric hindrance components of organic molecules, such as those
11
12 mimicked by the “pseudo DOM” RhB (see Fig. S1 and Text S10 in the Supporting Information).
13
14 However, because it is vastly more complex and variable, degradation of natural chromophoric
15
16 DOM by the same mechanism is less certain and requires direct testing. For our study, we chose to
17
18 examine terrestrial DOM from agricultural soil. Globally, approximately 0.25 Pg of dissolved
19
20 organic carbon (DOC) is transported annually from soils to ocean through riverine systems,^{56, 57}
21
22 especially in agricultural landscapes of the Midwest (e.g. Wisconsin and Michigan) where tile drains
23
24 are used to manage rainfed agriculture. Photodegradation is regarded as one of the major pathways
25
26 by which terrigenous DOM is decomposed. For instance, forest and grassland dominate drivers in
27
28 basins that lost up to 50% of DOC during irradiation.⁵⁸ In this scenario, DOM from agricultural soil
29
30 is exposed to sunlight when it enters the euphotic zone in rivers and is then decomposed through
31
32 photodegradation.⁵⁸ For our study, we examined water-extractable DOM from Wisconsin and
33
34 Michigan soil sites, characterizing them in molecular detail using multiple spectroscopic methods
35
36 including UV-vis absorption, FTICR-MS, ATR-FTIR, fluorescence, and 1D ¹H NMR spectroscopies
37
38 before and/or after the photoreaction in the presence of hematite and oxalate under light
39
40 illumination. The results and discussion of UV-vis absorption (Fig. S2A in the Supporting
41
42 Information) and FTICR-MS (Fig. S2B in the Supporting Information) of the pristine DOM
43
44 solutions are included in Text S11 of Supporting Information.
45
46
47
48
49
50
51
52
53
54
55
56

57
58 As is well known, oxalate is an extremely strong chelate reagent that could bind to the surface iron
59
60

1 active sites and then dissolve the hematite.^{33, 34} Different from oxalate, higher molecular weight
2
3 compounds in DOM that contain moieties such as long carbon chains would potentially sterically
4
5 hinder or otherwise diminish the efficacy of DOM-hematite interactions. Under this circumstance,
6
7 DOM could not compete with oxalate for surface iron active sites. As ROS were directly observed in
8
9 the presence of hematite nanoparticles and oxalate under light illumination (Figure 4), we
10
11 demonstrated that ROS are stable in the presence of oxalate and thus the quenchable effect of oxalate
12
13 on ROS consumption was negligible under current conditions. Overall, the influence of oxalate on
14
15 competitive adsorption for surface iron active sites and mineralization of DOM were safely
16
17 negligible.
18
19
20
21
22
23

24 ATR-FTIR spectroscopy was employed to investigate the change of the functional groups of
25
26 DOM before and after photoreaction with hematite and oxalate (Fig. 5A). The general IR spectral
27
28 profiles of DOM_{WS} and DOM_{MS} were similar but differ in the spectral details. For the natural
29
30 DOM, the broad peak at 3305 cm⁻¹ was assigned to amide NH or alcohol OH. In the region from
31
32 1800 cm⁻¹ to 1000 cm⁻¹, IR spectra displayed peaks corresponding to the organic functional groups,
33
34 including aromatic C=C and/or amide C=O (1655 cm⁻¹),⁵⁹ aliphatic CH₂ scissoring or in-plane
35
36 aromatic ring deformation (1492 cm⁻¹),⁵⁹ aliphatic CH₃ or acetyl CH₃ symmetry bend (1428
37
38 cm⁻¹),⁵⁹ phenol and/or carboxyl C-O or alkene C-N/C-H (1286 cm⁻¹),^{60, 61} and aliphatic C-C-O
39
40 stretching in ester (1187 cm⁻¹) and aliphatic O-C-C stretching in ester (1038 cm⁻¹).⁵⁹ The noticeable
41
42 peaks of the chromophoric DOM remained almost the same after the photochemical reaction, but
43
44 with careful observation they show small differences within the peaks in relation to the unreacted
45
46 ones, confirming the bleachability of the chromophoric DOM. For instance, the prominent peak at
47
48 1655 cm⁻¹ for DOM_{MS} was slightly decreased due to the degradation of the aromatic C=C and/or
49
50 amide C=O functional groups and the depolymerization of the organics in DOM_{MS} (Fig. S3 in the
51
52
53
54
55
56
57
58
59
60

1 Supporting Information).

2
3
4 The fluorescence emission spectra showed a broad band at around 400-550 nm (Fig. 5B), typical
5
6 of humic-like fluorophores.⁶² The intensity at 440 nm after reaction was respectively reduced
7
8 24.9% and 51.8% for DOM_{WS} and DOM_{MS}, revealing that both of them were efficiently bleached
9
10 by the hydroxyl radicals. Obviously, the main peaks became broad and had hypsochromic shifts in
11
12 emission wavelength after the photoreaction (especially for DOM_{MS}), likely due to the formation of
13
14 new fluorophores.
15
16
17

18
19 We measured the DOC change of DOM as a function of reaction time in the presence of hematite
20
21 and oxalate under illumination (Fig. 5C). As expected, the DOC values of DOM_{WS} and DOM_{MS}
22
23 decreased as a function of reaction time, indicating that the organic carbon of DOM was mineralized
24
25 into inorganic carbon species, such as CO₂. The chamber used to expose samples to the light source
26
27 is not equipped to directly measure CO₂ evolution in the headspace. The TOC measurements on both
28
29 DOM samples following light exposure showed a decrease in concentration relative to their
30
31 respective unexposed controls. As CO₂ generation is the only known pathway to release carbon from
32
33 DOM under oxic conditions, the drop in TOC concentrations in the exposed DOM extracts suggests
34
35 an efficient release of CO₂. The degradation rate constants were calculated to be 7.94 and 4.50 mg
36
37 L⁻¹ h⁻¹ with coefficients of determination (R²) of 0.51 and 0.71 for DOM_{WS} and DOM_{MS},
38
39 respectively. The degradation rate constant of DOM_{WS} was 1.76 times than DOM_{MS}, likely because
40
41 DOM_{WS} is endowed with higher organic chromophore content relative to DOM_{MS}.
42
43
44
45
46
47
48
49

50
51 1D ¹H NMR spectroscopy was also used to characterize the water extracted DOM samples after
52
53 exposure to 5 hours of light in the presence of hematite nanoparticles and oxalate along with
54
55 identically prepared controls not exposed to light (for consistency, controls and exposed samples will
56
57 be referred to as “before” and “after” respectively). The extracts were concentrated by lyophilization
58
59
60

1 prior to measurement, reconstituted in D₂O, and the spectra are shown in Figure 5D. General
2
3 comparisons were made by dividing each spectrum into five specific chemical shift regions,
4
5 corresponding to common structural moieties present within, and integrating their areas to yield
6
7 comparative proportions of each type as in Hertkorn et al.^{63, 64} Specifically, the structural types and
8
9 ¹H chemical shift ranges employed were 1) aliphatics (CCCH) from 0.5 – 1.9 ppm, a region which
10
11 may contain significant contributions from compounds that were mainly derived from linear
12
13 terpenoids (MDLT) as noted by Lam et al.⁶⁵; 2) functionalized aliphatics (XCCH, X = O, N, or S,⁶⁴
14
15 or NCH of primary and secondary amines) from 1.9 – 3.1 ppm, wherein other studies have noted
16
17 major refractory components for DOM in this region to be attributable to compounds such as
18
19 carboxylic-rich alicyclic molecules (CRAM)⁶⁶ and oxidized sterols⁶⁷ as two examples; 3)
20
21 oxygenated (OCH) type resonances from 3.1 – 4.5 ppm that would encompass carbohydrates but
22
23 also C_α protons of amino acids; 4) unsaturated/olefinic (HC=C) from 5.3 – 7.0 ppm, with some
24
25 overlap from carbohydrate anomeric protons (O₂CH) and 5) aromatics/heteroaromatics (HC_{aromatic})
26
27 from 7.0 – 10.0 ppm.⁶³ The region between 4.5 – 5.3 ppm was not integrated due to suppression of
28
29 the residual water signal (approx. 4.7 ppm). The integration results indicating the percent
30
31 contribution of the integrated region to the total integrated area of each spectrum as well as relative
32
33 percent differences before and after exposure are compiled in Table 1 below. Profiles of the DOM
34
35 regions were roughly similar for DOM_{WS} and DOM_{MS} and both showed notable changes in all
36
37 regions including decreasing intensity in aromatic (HC_{aromatic}), olefinic/anomeric (HC=C/O₂CH), and
38
39 oxygenated (CHO) regions with concomitant increases in the functionalized (XCCH) and aliphatic
40
41 (CCCH) regions. The DOM_{MS} sample showed greater relative percent changes in every region
42
43 relative to DOM_{WS}. With respect to the aromatic region, in particular, not only was there a clear
44
45 decrease in overall intensity and loss of the few sharper features (especially DOM_{MS}) but resonances
46
47
48
49
50
51
52
53
54
55
56
57
58
59
60

1 with shifts consistent with aldehydes (ca. 9.7 ppm) also appear in both light exposed DOM samples
2
3 versus the unexposed controls. The olefinic/O₂CH regions overall decreased, however there was an
4
5 apparent slight increase in intensity at the lower chemical shift end of the range (ca. 5.6 – 5.3 ppm)
6
7 in both exposed DOM samples. The net increases in intensity for the functionalized aliphatics
8
9 (XCCH) and aliphatics (CCCH) were punctuated by several new intense and narrower resonances
10
11 appearing in both DOM samples after exposure that, although no specific compound identifications
12
13 were made in the post-exposure samples in this region, were consistent with the formation of long
14
15 chain aliphatics with carboxylic or amino functional groups.
16
17
18
19
20

21 The NMR data is consistent with the ATR-FTIR results in supporting predictions that aromatic
22
23 and unsaturated functional groups would be predominantly degraded by reaction with hydroxyl
24
25 radicals as a likely consequence of their electron rich properties. Because aromatic functional groups
26
27 represent large molecular weight compounds, such as lignin, and aliphatic carbon chains refers to
28
29 LMW compounds (relatively lower molecular weight organics than original counterparts caused by
30
31 oxidation), like hydrocarbons. As reaction goes by, the LMW organic compounds were further
32
33 mineralized into inorganic species, such as carbon dioxide which has been regarded as the only
34
35 pathway to release carbon from DOM samples under oxic conditions. Therefore, the possible
36
37 degradation pathway of DOM was summarized below. The aromatic and unsaturated functional
38
39 groups were predominantly attacked by hydroxyl radicals to form LMW organic compounds and
40
41 further mineralized into inorganic species, such as carbon dioxide.
42
43
44
45
46
47
48
49

50 On the basis of the efficient degradation of both DOM_{WS} and DOM_{MS} above, our findings
51
52 indicate that, like the proxy molecule RhB, DOM extracted from agricultural soil is also indirectly
53
54 photobleached by the hydroxyl free radicals produced by the photocatalyzed LMCT reaction at
55
56 oxalate functionalized hematite nanoplate surfaces. The broadly consistent mechanism appears to
57
58
59
60

1 be electrophilic attack of the electron-rich functional groups (e.g., aromatic rings, conjugated alkyl
2
3 and hydroxyl groups) that rapidly decompose into LMW organic substances, and/or are further
4
5 mineralized into inorganic species such as CO₂. Although it has been previously shown that oxalate
6
7
8 can comprise one of these LMW products,²⁵ hence raising the prospect that regeneration of oxalate
9
10 might in turn accelerate the photodegradation of DOM concertededly, the present experiments did not
11
12 enable us to detect oxalate release. In any event, the overall photodegradation process observed in
13
14 this study can be succinctly summarized by the reaction:
15
16
17



18
19
20
21 It is known that oxalate is the smallest LMW dicarboxylic acid, a plant exudate, a possible
22
23 degradation intermediate from the oxidation of natural organic matter, and thus abundant in soil and
24
25 near-surface terrestrial aquatic environments. Oxalate that binds to hematite nanoparticles can
26
27 photocatalyze the production of ROS through interfacial electron transfer and valence cycling of iron
28
29 sites at the interface. Although the photochemistry of hematite or oxalate for the generation of ROS
30
31 has been extensively studied, the photodegradation of DOM by hematite nanoplates functionalized
32
33 by adsorbed oxalate has long been overlooked due to the complexity of natural DOM samples.
34
35 Additionally, in natural ecosystems multiple DOM degradation mechanisms may occur, including
36
37 enzymatic degradation, which is regarded as the main biotic degradation pathway.⁶⁸ Therefore,
38
39 DOM degradation products measured in environmental samples may reflect multiple degradation
40
41 pathways. Thus, model systems using laboratory-synthesized hematite can help isolate the process of
42
43
44
45
46
47
48
49
50
51 DOM degradation by ROS.

52
53 In designing such a model experimental system, it is important to consider its composition with
54
55 respect to real soils, while also maintaining conditions that are practical for laboratory-based
56
57 measurements. The concentration of oxalate ranged from several micromolar per liter to hundreds of
58
59
60

1 millimolar per liter, such as 2.0-550 μM in soils⁶⁹ and ever higher as 11.7 mM in the atmospheric
2
3
4 dust.⁷⁰ In the present study, we used 1.0 g/L of hematite (approximately from 1.9-500 g of soil based
5
6 on hematite contents in natural soils ranging from approximately 0.1-26 g/kg)⁷¹ and 1.0 mM of
7
8 oxalate by mixing hematite nanoparticles and oxalate with DOM solution extracted from soils. The
9
10 concentration of oxalate employed in our laboratory investigation is thus comparable to natural
11
12 environmental conditions. And because the role of hematite in isolation is the focus of the study its
13
14 concentration was chosen to be comparable with other studies using synthesized hematite for
15
16 simulating real environmental conditions.^{4, 30}
17
18
19
20
21

22 **4. Conclusions**

23
24 Iron oxides, organic ligands, and chromophoric DOM are important components in soils, and
25
26 common in the euphotic zone of lacustrine and marine environments where solar photogeochemical
27
28 carbon cycling occurs. We have examined one possible indirect DOM photodegradation pathway
29
30 that is based on light-induced reactive oxygen species production at hematite nanoparticles coated
31
32 with oxalate surface complexes. Light catalyzes ligand-to-metal charge transfer from the adsorbed
33
34 oxalate to Fe(III) in the particles, creating a supply of Fe(II) associated with photodissolution of
35
36 particle surfaces. At the same time, the key oxalate photolysis product is the carboxyl anion radical
37
38 $\bullet\text{CO}_2^-$, which readily reduces dissolved oxygen to yield a supply of H_2O_2 . The interaction of Fe(II)
39
40 and H_2O_2 leads to hydroxyl radical production via the canonical Fenton reactions that cycle Fe
41
42 valence, which efficiently degrades the pseudo-DOM chromophore RhB as well as model natural
43
44 chromophoric DOM compounds from agricultural soil. The findings suggest that this indirect DOM
45
46 photodegradation pathway could be significant in natural aquatic systems where these components
47
48 pervade, adding a controlling process to the total DOM pool in euphotic zones and thereby
49
50 impacting the global carbon cycle. The same process may likewise be relevant to the fate of organic
51
52
53
54
55
56
57
58
59
60

1 micropollutants in these settings. The findings also add mechanistic understanding to factors
2
3
4 controlling steady-state concentrations of environmentally persistent ROS, through its coupling to
5
6 natural organic matter cycling and, in turn, terrestrial ecosystems.
7
8
9

10 11 **Supporting Information**

12
13
14 The Supporting Information is available on the RSC website: Materials (Text S1), Synthesis of
15
16 hematite nanoplates (Text S2), Characterization (Text S3), Analytical methods (Text S4), EPR
17
18 spectroscopy (Text S5), Natural DOM extraction (Text S6), FTICR MS data acquisition and data
19
20 analysis (Text S7), Nuclear magnetic resonance spectroscopy (Text S8), Photodegradation
21
22 experiments (Text S9), Photodegradation of RhB (Text S10), DOM characterizations (Text S11), ,
23
24 Photodegradation of RhB and scavenger experiments (Figure S1), DOM characterizations (Figure
25
26 S2), The magnified ATR-FTIR spectra of DOM_{MS} (Figure S3), and Defect analyses (Table S1).
27
28
29
30
31
32
33
34

35 **Statement of contributions**

36
37 X.H. and K.M.R. designed the research. X.H. synthesized the nanoparticles, conducted the
38
39 photodissolution and DOM photodegradation experiments. Q.Z. and K.H. extracted the DOM
40
41 solutions and conducted TOC and FTICR-MS analysis. R.Y. conducted the NMR and analysis. X.Z.
42
43 conducted the TEM and STEM and E.N analyzed the images. X.H., E.W. and Y.C. conducted the
44
45 EPR and analysis. X.H. and S.T. analyzed the dissolution and characterization. X.H. and J.L.
46
47 performed the ATR-FTIR. X.H. and Z.W. performed the fluorescence spectra. All the coauthors
48
49
50
51
52
53 co-wrote the manuscript.
54
55
56
57

58 **Conflicts of interest**

59
60

1 There are no conflicts of interest to declare.
2
3
4
5

6 **Acknowledgements** 7

8 This work was supported by the U.S. Department of Energy (DOE), Office of Science, Office of
9 Basic Energy Sciences (BES), Chemical Sciences, Geosciences, and Biosciences Division through
10 its Geosciences program at Pacific Northwest National Laboratory (PNNL). A portion of the
11 research was performed using EMSL (grid.436923.9), a DOE Office of Science User Facility
12 sponsored by the Office of Biological and Environmental Research and is located at PNNL. PNNL is
13 a multiprogram national laboratory operated for DOE by Battelle under Contract No.
14 DE-AC05-76RL01830.
15
16
17
18
19
20
21
22
23
24
25
26
27
28
29
30
31
32
33
34
35
36
37
38
39
40
41
42
43
44
45
46
47
48
49
50
51
52
53
54
55
56
57
58
59
60

References

1. M. F. Hochella, Jr., D. W. Mogk, J. Ranville, I. C. Allen, G. W. Luther, L. C. Marr, B. P. McGrail, M. Murayama, N. P. Qafoku, K. M. Rosso, N. Sahai, P. A. Schroeder, P. Vikesland, P. Westerhoff and Y. Yang, Natural, incidental, and engineered nanomaterials and their impacts on the Earth system, *Science*, 2019, **363**, eaau8299.
2. M. F. Hochella, S. K. Lower, P. A. Maurice, R. L. Penn, N. Sahai, D. L. Sparks and B. S. Twining, Nanominerals, mineral nanoparticles, and Earth systems, *Science*, 2008, **319**, 1631-1635.
3. X. Huang, X. Hou, X. Zhang, K. M. Rosso and L. Zhang, Facet-dependent contaminant removal properties of hematite nanocrystals and their environmental implications, *Environ. Sci.: Nano*, 2018, **5**, 1790-1806.
4. X. Huang, X. Hou, F. Song, J. Zhao and L. Zhang, Facet-dependent Cr(VI) adsorption of hematite nanocrystals, *Environ. Sci. Technol.*, 2016, **50**, 1964-1972.
5. E. D. Melton, E. D. Swanner, S. Behrens, C. Schmidt and A. Kappler, The interplay of microbially mediated and abiotic reactions in the biogeochemical Fe cycle, *Nat. Rev. Microbiol.*, 2014, **12**, 797-808.
6. X. Huang, X. Hou, F. Wang, B. Guo, F. Song, L. Ling, J. Zhao and L. Zhang, Molecular-scale structures of uranyl surface complexes on hematite facets, *Environ. Sci.: Nano*, 2019, **6**, 892-903.
7. P. G. Falkowski, Evolution of the nitrogen cycle and its influence on the biological sequestration of CO₂ in the ocean, *Nature*, 1997, **387**, 272.
8. P. G. Falkowski, R. T. Barber and V. Smetacek, Biogeochemical Controls and Feedbacks on Ocean Primary Production, *Science*, 1998, **281**, 200-206.

- 1 9. F. Morel and N. Price, The biogeochemical cycles of trace metals in the oceans, *Science*,
2
3 2003, **300**, 944-947.
- 4
5
6 10. T. Borch, R. Kretzschmar, A. Kappler, P. V. Cappellen, M. Ginder-Vogel, A. Voegelin and
7
8 K. Campbell, Biogeochemical redox processes and their impact on contaminant dynamics,
9
10 *Environ. Sci. Technol.*, 2010, **44**, 15-23.
- 11
12
13 11. X. Huang, X. Hou, F. Jia, F. Song, J. Zhao and L. Zhang, Ascorbate-promoted surface iron
14
15 cycle for efficient heterogeneous Fenton alachlor degradation with hematite nanocrystals,
16
17 *ACS Appl. Mater. Interfaces*, 2017, **9**, 8751-8758.
- 18
19
20 12. X. Huang, X. Hou, J. Zhao and L. Zhang, Hematite facet confined ferrous ions as high
21
22 efficient Fenton catalysts to degrade organic contaminants by lowering H₂O₂ decomposition
23
24 energetic span, *Appl. Catal., B*, 2016, **181**, 127-137.
- 25
26
27 13. K. Barbeau, E. Rue, K. Bruland and A. Butler, Photochemical cycling of iron in the surface
28
29 ocean mediated by microbial iron (III)-binding ligands, *Nature*, 2001, **413**, 409-413.
- 30
31
32 14. X. Huang, X. Hou, F. Song, J. Zhao and L. Zhang, Ascorbate induced facet dependent
33
34 reductive dissolution of hematite nanocrystals, *J. Phys. Chem. C*, 2017, **121**, 1113-1121.
- 35
36
37 15. P. W. Boyd, A. J. Watson, C. S. Law, E. R. Abraham, T. Trull, R. Murdoch, D. C. E. Bakker,
38
39 A. R. Bowie, K. O. Buesseler, H. Chang, M. Charette, P. Croot, K. Downing, R. Frew, M.
40
41 Gall, M. Hadfield, J. Hall, M. Harvey, G. Jameson, J. LaRoche, M. Liddicoat, R. Ling, M. T.
42
43 Maldonado, R. M. McKay, S. Nodder, S. Pickmere, R. Pridmore, S. Rintoul, K. Safi, P.
44
45 Sutton, R. Strzeppek, K. Tanneberger, S. Turner, A. Waite and J. Zeldis, A mesoscale
46
47 phytoplankton bloom in the polar Southern Ocean stimulated by iron fertilization, *Nature*,
48
49 2000, **407**, 695-702.
- 50
51
52 16. V. Smetacek, C. Klaas, V. H. Strass, P. Assmy, M. Montresor, B. Cisewski, N. Savoye, A.
53
54
55
56
57
58
59
60

- 1 Webb, F. d'Ovidio, J. M. Arrieta, U. Bathmann, R. Bellerby, G. M. Berg, P. Croot, S.
2
3 Gonzalez, J. Henjes, G. J. Herndl, L. J. Hoffmann, H. Leach, M. Losch, M. M. Mills, C.
4
5 Neill, I. Peeken, R. Rottgers, O. Sachs, E. Sauter, M. M. Schmidt, J. Schwarz, A. Terbruggen
6
7 and D. Wolf-Gladrow, Deep carbon export from a Southern Ocean iron-fertilized diatom
8
9 bloom, *Nature*, 2012, **487**, 313-319.
10
11
12
13
14 17. D. E. Latch and K. McNeill, Microheterogeneity of singlet oxygen distributions in irradiated
15
16 humic acid solutions, *Science*, 2006, **311**, 1743-1747.
17
18
19 18. A. Nebbioso and A. Piccolo, Molecular characterization of dissolved organic matter (DOM):
20
21 a critical review, *Anal. Bioanal. Chem.*, 2013, **405**, 109-124.
22
23
24 19. J. P. Hassett, Dissolved Natural Organic Matter as a Microreactor, *Science*, 2006, **311**,
25
26 1723-1724.
27
28
29 20. Q. Lan, F. Li, C. Liu and X.-Z. Li, Heterogeneous Photodegradation of Pentachlorophenol
30
31 with Maghemite and Oxalate under UV Illumination, *Environ. Sci. Technol.*, 2008, **42**,
32
33 7918-7923.
34
35
36
37 21. Q. Lan, F.-b. Li, C.-x. Sun, C.-s. Liu and X.-z. Li, Heterogeneous photodegradation of
38
39 pentachlorophenol and iron cycling with goethite, hematite and oxalate under UVA
40
41 illumination, *J. Hazard. Mater.*, 2010, **174**, 64-70.
42
43
44
45 22. M. Huang, W. Xiang, T. Zhou, J. Mao, X. Wu and X. Guo, The critical role of the surface
46
47 iron-oxalate complexing species in determining photochemical degradation of norfloxacin
48
49 using different iron oxides, *Sci. Total Environ.*, 2019, **697**, 134220.
50
51
52
53 23. M. E. Balmer and B. Sulzberger, Atrazine Degradation in Irradiated Iron/Oxalate Systems:
54
55 Effects of pH and Oxalate, *Environ. Sci. Technol.*, 1999, **33**, 2418-2424.
56
57
58 24. P. Behra and L. Sigg, Evidence for redox cycling of iron in atmospheric water droplets,
59
60

- 1 *Nature*, 1990, **344**, 419-421.
- 2
- 3
- 4 25. S. Sabine, S. G. Huber, K. Karsten and H. F. Schöler, Natural abiotic formation of oxalic
- 5 acid in soils: results from aromatic model compounds and soil samples, *Environ. Sci.*
- 6 *Technol.*, 2013, **47**, 1323-1329.
- 7
- 8
- 9
- 10
- 11 26. Z. Wang, X. Chen, H. Ji, W. Ma, C. Chen and J. Zhao, Photochemical Cycling of Iron
- 12 Mediated by Dicarboxylates: Special Effect of Malonate, *Environ. Sci. Technol.*, 2010, **44**,
- 13 263-268.
- 14
- 15
- 16
- 17
- 18
- 19 27. B. M. Voelker, F. M. M. Morel and B. Sulzberger, Iron Redox Cycling in Surface Waters:
- 20 Effects of Humic Substances and Light, *Environ. Sci. Technol.*, 1997, **31**, 1004-1011.
- 21
- 22
- 23
- 24 28. B. Sulzberger and E. Durisch-Kaiser, Chemical characterization of dissolved organic matter
- 25 (DOM): A prerequisite for understanding UV-induced changes of DOM absorption
- 26 properties and bioavailability, *Aquat. Sci.*, 2009, **71**, 104-126.
- 27
- 28
- 29
- 30
- 31
- 32 29. K. Mopper and X. Zhou, Hydroxyl Radical Photoproduction in the Sea and Its Potential
- 33 Impact on Marine Processes, *Science*, 1990, **250**, 661-664.
- 34
- 35
- 36
- 37 30. X. Huang, Y. Chen, E. Walter, M. Zong, Y. Wang, X. Zhang, O. Qafoku, Z. Wang and K. M.
- 38 Rosso, Facet-Specific Photocatalytic Degradation of Organics by Heterogeneous Fenton
- 39 Chemistry on Hematite Nanoparticles, *Environ. Sci. Technol.*, 2019, **53**, 10197-10207.
- 40
- 41
- 42
- 43
- 44
- 45 31. L. Chen, X. Yang, J. Chen, J. Liu, H. Wu, H. Zhan, C. Liang and M. Wu, Continuous shape-
- 46 and spectroscopy-tuning of hematite nanocrystals, *Inorg. Chem.*, 2010, **49**, 8411-8420.
- 47
- 48
- 49
- 50 32. M. L. Liu, X. A. Mao, C. H. Ye, H. Huang, J. K. Nicholson and J. C. Lindon, Improved
- 51 WATERGATE pulse sequences for solvent suppression in NMR spectroscopy, *J. Magn.*
- 52 *Reson.*, 1998, **132**, 125-129.
- 53
- 54
- 55
- 56
- 57
- 58 33. J. S. Loring, A. A. Simanova and P. Persson, Highly Mobile Iron Pool from a
- 59
- 60

- 1 Dissolution–Readsorption Process, *Langmuir*, 2008, **24**, 7054-7057.
- 2
- 3
- 4 34. P. Persson and K. Axe, Adsorption of oxalate and malonate at the water-goethite interface:
- 5
- 6 Molecular surface speciation from IR spectroscopy, *Geochim. Cosmochim. Acta*, 2005, **69**,
- 7
- 8 541-552.
- 9
- 10
- 11 35. D. M. Mangiante, R. D. Schaller, P. Zarzycki, J. F. Banfield and B. Gilbert, Mechanism of
- 12
- 13 Ferric Oxalate Photolysis, *ACS Earth Space Chem.*, 2017, **1**, 270-276.
- 14
- 15
- 16 36. D. Panias, M. Taxiarchou, I. Paspaliaris and A. Kontopoulos, Mechanisms of dissolution of
- 17
- 18 iron oxides in aqueous oxalic acid solutions, *Hydrometallurgy*, 1996, **42**, 257-265.
- 19
- 20
- 21 37. D. Panias, M. Taxiarchou, I. Douni, I. Paspaliaris and A. Kontopoulos, Dissolution of
- 22
- 23 hematite in acidic oxalate solutions: the effect of ferrous ions addition, *Hydrometallurgy*,
- 24
- 25 1996, **43**, 219-230.
- 26
- 27
- 28
- 29 38. X. Hou, X. Huang, F. Jia, Z. Ai, J. Zhao and L. Zhang, Hydroxylamine promoted goethite
- 30
- 31 surface Fenton degradation of organic pollutants, *Environ. Sci. Technol.*, 2017, **51**,
- 32
- 33 5118-5126.
- 34
- 35
- 36
- 37 39. D. A. Wheeler, G. M. Wang, Y. C. Ling, Y. Li and J. Z. Zhang, Nanostructured hematite:
- 38
- 39 synthesis, characterization, charge carrier dynamics, and photoelectrochemical properties,
- 40
- 41 *Energy Environ. Sci.*, 2012, **5**, 6682-6702.
- 42
- 43
- 44
- 45 40. J. Deng, X. Lv, J. Gao, A. Pu, M. Li, X. Sun and J. Zhong, Facile synthesis of carbon-coated
- 46
- 47 hematite nanostructures for solar water splitting, *Energy Environ. Sci.*, 2013, **6**, 1965-1970.
- 48
- 49
- 50 41. R. Bianchini, L. Calucci, C. Lubello and C. Pinzino, Intermediate free radicals in the
- 51
- 52 oxidation of wastewaters, *Res. Chem. Intermed.*, 2002, **28**, 247-256.
- 53
- 54
- 55 42. F. A. Villamena, E. J. Locigno, A. Rockenbauer, C. M. Hadad and J. L. Zweier, Theoretical
- 56
- 57 and Experimental Studies of the Spin Trapping of Inorganic Radicals by
- 58
- 59
- 60

- 1 5,5-Dimethyl-1-Pyrroline N-Oxide (DMPO). 1. Carbon Dioxide Radical Anion, *J. Phys.*
2
3
4 *Chem. A*, 2006, **110**, 13253-13258.
5
- 6 43. I. R. Cohen, T. C. Purcell and A. P. Altshuller, Analysis of the oxidant in photooxidation
7
8 reactions, *Environ. Sci. Technol.*, 1967, **1**, 247-252.
9
- 10
11 44. S. J. Hug, H.-U. Laubscher and B. R. James, Iron(III) Catalyzed Photochemical Reduction of
12
13 Chromium(VI) by Oxalate and Citrate in Aqueous Solutions, *Environ. Sci. Technol.*, 1997,
14
15 **31**, 160-170.
16
17
- 18
19 45. P. S. Surdhar, S. P. Mezyk and D. A. Armstrong, Reduction potential of the carboxyl radical
20
21 anion in aqueous solutions, *J. Phys. Chem.*, 1989, **93**, 3360-3363.
22
23
- 24
25 46. L. L. Perissinotti, M. A. Brusa and M. A. Grela, Yield of Carboxyl Anion Radicals in the
26
27 Photocatalytic Degradation of Formate over TiO₂ Particles, *Langmuir*, 2001, **17**, 8422-8427.
28
29
- 30
31 47. J. J. Warren, T. A. Tronic and J. M. Mayer, Thermochemistry of Proton-Coupled Electron
32
33 Transfer Reagents and its Implications, *Chem. Rev.*, 2010, **110**, 6961-7001.
34
35
- 36
37 48. J. Rosenthal and D. G. Nocera, Role of Proton-Coupled Electron Transfer in O–O Bond
38
39 Activation, *Acc. Chem. Res.*, 2007, **40**, 543-553.
40
41
- 42
43 49. Y. Zuo and J. Hoigne, Formation of hydrogen peroxide and depletion of oxalic acid in
44
45 atmospheric water by photolysis of iron(III)-oxalato complexes, *Environ. Sci. Technol.*,
46
47 1992, **26**, 1014-1022.
48
49
- 50
51 50. Y. Zuo and J. Hoigné, Evidence for Photochemical Formation of H₂O₂ and Oxidation of SO₂
52
53 in Authentic Fog Water, *Science*, 1993, **260**, 71-73.
54
55
- 56
57 51. Y. Ilan and J. Rabani, On some fundamental reactions in radiation chemistry: Nanosecond
58
59 pulse radiolysis, *Int. J. Radiat. Phys. Chem.*, 1976, **8**, 609-611.
60
- 60
61

- 1 hydroxyl radical by 6-hydroxydopamine, dialuric acid, and related cytotoxic agents, *J. Biol.*
2
3
4 *Chem.*, 1974, **249**, 2447-2452.
- 5
6 53. A. E. Dikalova, M. B. Kadiiska and R. P. Mason, An *in vivo* ESR spin-trapping study: Free
7
8 radical generation in rats from formate intoxication— role of the Fenton reaction, *Proc. Natl.*
9
10 *Acad. Sci. U.S.A.*, 2001, **98**, 13549-13553.
- 11
12
13 54. G. V. Buxton, C. L. Greenstock, W. P. Helman and A. B. Ross, Critical Review of rate
14
15 constants for reactions of hydrated electrons, hydrogen atoms and hydroxyl radicals
16
17 ($\bullet\text{OH}/\bullet\text{O}^-$) in Aqueous Solution, *J. Phys. Chem. Ref. Data*, 1988, **17**, 513-886.
- 18
19
20 55. F. Haber, J. Weiss and W. J. Pope, The catalytic decomposition of hydrogen peroxide by iron
21
22 salts, *J. Proc. R. Soc. Ser.*, 1934, **147**, 332-351.
- 23
24
25 56. J. I. Hedges, R. G. Keil and R. Benner, What happens to terrestrial organic matter in the
26
27 ocean?, *Org. Geochem.*, 1997, **27**, 195-212.
- 28
29
30 57. M. Dai, Z. Yin, F. Meng, Q. Liu and W.-J. Cai, Spatial distribution of riverine DOC inputs to
31
32 the ocean: an updated global synthesis, *Curr. Opin. Environ. Sustain.*, 2012, **4**, 170-178.
- 33
34
35 58. T. Riedel, M. Zark, A. V. Vähätalo, J. Niggemann, R. G. M. Spencer, P. J. Hernes and T.
36
37 Dittmar, Molecular Signatures of Biogeochemical Transformations in Dissolved Organic
38
39 Matter from Ten World Rivers, *Front. Earth Sci.*, 2016, **4**.
- 40
41
42 59. H. A. N. Abdulla, E. C. Minor, R. F. Dias and P. G. Hatcher, Changes in the compound
43
44 classes of dissolved organic matter along an estuarine transect: A study using FTIR and ^{13}C
45
46 NMR, *Geochim. Cosmochim. Acta*, 2010, **74**, 3815-3838.
- 47
48
49 60. A. J. Margenot, F. J. Calderón, K. W. Goyne, F. N. D. Mukome and S. J. Parikh, in
50
51
52 *Encyclopedia of Spectroscopy and Spectrometry (Third Edition)*, eds. J. C. Lindon, G. E.
53
54 Tranter and D. W. Koppenaal, Academic Press, Oxford, 2017, DOI:
55
56
57
58
59
60

<https://doi.org/10.1016/B978-0-12-409547-2.12170-5>, pp. 448-454.

61. A. B. A. Daoud and L. Tremblay, HPLC-SEC-FTIR characterization of the dissolved organic matter produced by the microbial carbon pump, *Mar. Chem.*, 2019, **215**, 103668.
62. N. Hudson, A. Baker and D. Reynolds, Fluorescence analysis of dissolved organic matter in natural, waste and polluted waters—a review, *River Res. Appl.*, 2007, **23**, 631-649.
63. N. Hertkorn, M. Harir, B. Koch, B. Michalke and P. Schmitt-Kopplin, High-field NMR spectroscopy and FTICR mass spectrometry: powerful discovery tools for the molecular level characterization of marine dissolved organic matter, *Biogeosciences*, 2013, **10**, 1583-1624.
64. Y. Li, M. Harir, M. Lucio, B. Kanawati, K. Smirnov, R. Flerus, B. P. Koch, P. Schmitt-Kopplin and N. Hertkorn, Proposed Guidelines for Solid Phase Extraction of Suwannee River Dissolved Organic Matter, *Anal. Chem.*, 2016, **88**, 6680-6688.
65. B. Lam, A. Baer, M. Alaei, B. Lefebvre, A. Moser, A. Williams and A. J. Simpson, Major structural components in freshwater dissolved organic matter, *Environ. Sci. Technol.*, 2007, **41**, 8240-8247.
66. N. Hertkorn, R. Benner, M. Frommberger, P. Schmitt-Kopplin, M. Witt, K. Kaiser, A. Kettrup and J. I. Hedges, Characterization of a major refractory component of marine dissolved organic matter, *Geochim. Cosmochim. Acta*, 2006, **70**, 2990-3010.
67. G. C. Woods, M. J. Simpson and A. J. Simpson, Oxidized sterols as a significant component of dissolved organic matter: Evidence from 2D HPLC in combination with 2D and 3D NMR spectroscopy, *Water Res.*, 2012, **46**, 3398-3408.
68. R. J. Chróst, in *Aquat. Microb. Ecol.*, Springer, 1990, pp. 47-78.
69. D. L. Jones, Organic acids in the rhizosphere – a critical review, *Plant Soil*, 1998, **205**, 25-44.

- 1 70. H. Chen and V. H. Grassian, Iron dissolution of dust source materials during simulated acidic
2
3 processing: The effect of sulfuric, acetic, and oxalic acids, *Environ. Sci. Technol.*, 2013, **47**,
4
5 10312-10321.
6
7
- 8 71. J. Torrent, U. Schwertmann, H. Fechter and F. Alferez, Quantitative relationships between
9
10 soil color and hematite content, *Soil Sci.*, 1983, **136**, 354-358.
11
12
13
14
15
16
17
18
19
20
21
22
23
24
25
26
27
28
29
30
31
32
33
34
35
36
37
38
39
40
41
42
43
44
45
46
47
48
49
50
51
52
53
54
55
56
57
58
59
60

FIGURES AND CAPTIONS

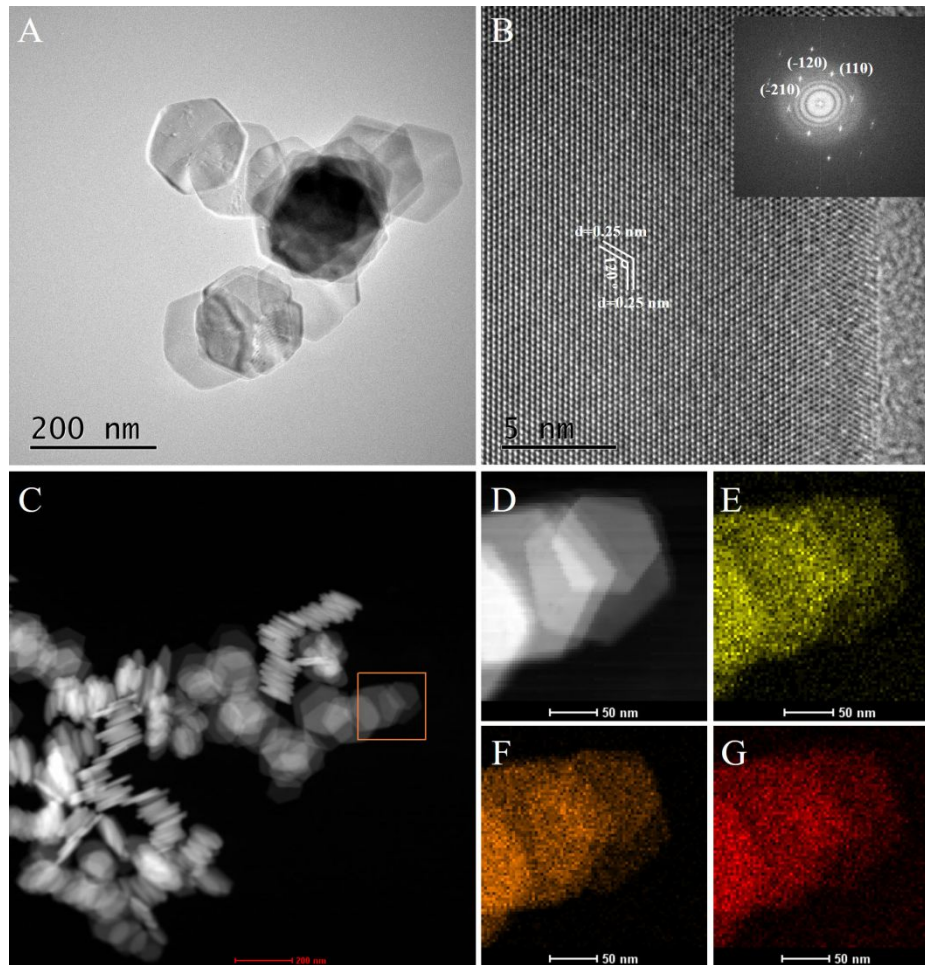


Figure 1. Representative morphologies and structures of hematite nanoplates. (A) TEM image, (B) high-resolution TEM image and corresponding SAED pattern (Insert), (C) drift corrected spectrum image scanning of HADDF-STEM, (D) selected area of HADDF-STEM, (E) Fe L-edge mapping, (F) Fe K-edge mapping, and (G) O K-edge mapping of hematite nanoplates.

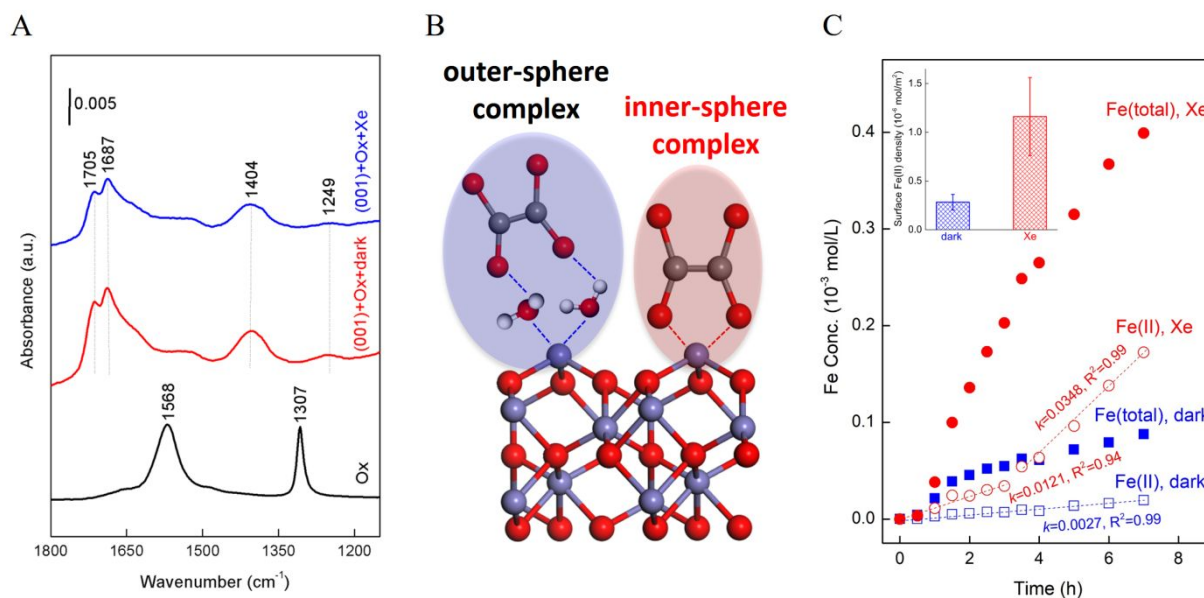


Figure 2. (A) ATR-FTIR spectroscopy of hematite after photoreaction in the presence and in the absence of light illumination. (B) The possible molecular structures of outer-sphere and inner-sphere complexes of iron-oxalate on hematite (001) surface with Fe-terminations. (C) The reductive dissolution kinetics of hematite with oxalate versus photoreaction time in the presence and in the absence of light illumination (Insert: corresponding surface Fe(II) density on hematite). k and R^2 were the pseudo-zero-order-rate constants of photoproduction of Fe(II) in the solution and the corresponding fitting correlation coefficient values, respectively.

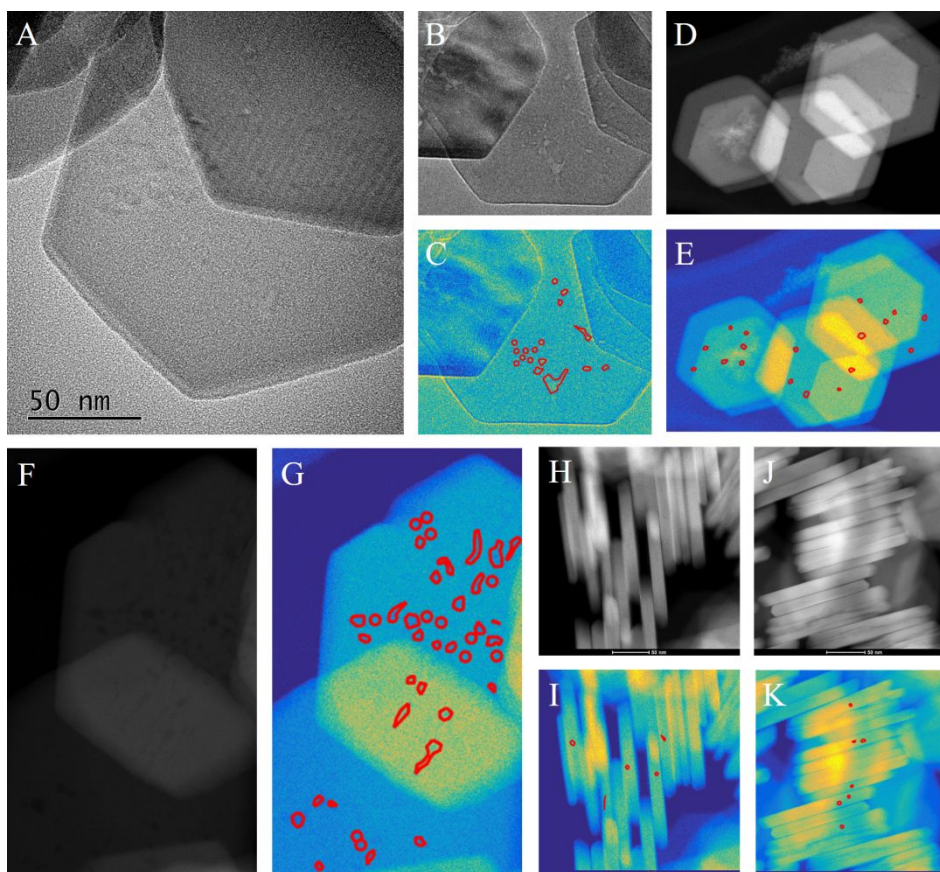


Figure 3. TEM and HADDF-STEM imaging and defect analysis of hematite nanoplates before and after the photochemical reaction in the presence of oxalate. (A) TEM images showing the hematite basal (001) surface before reaction, (B)-(C) TEM images of hematite basal (001) surface after reaction. (D)-(E) HADDF-STEM images showing the hematite basal (001) surface before reaction, (F)-(G) HADDF-STEM images of hematite basal (001) surface after reaction. (H)-(I) HADDF-STEM images showing the hematite edge (012) surface before reaction, (J)-(K) HADDF-STEM images showing the hematite edge (012) surface after reaction. The colored images displayed the defects of basal (001) and edge (012) surface on hematite nanoplates.

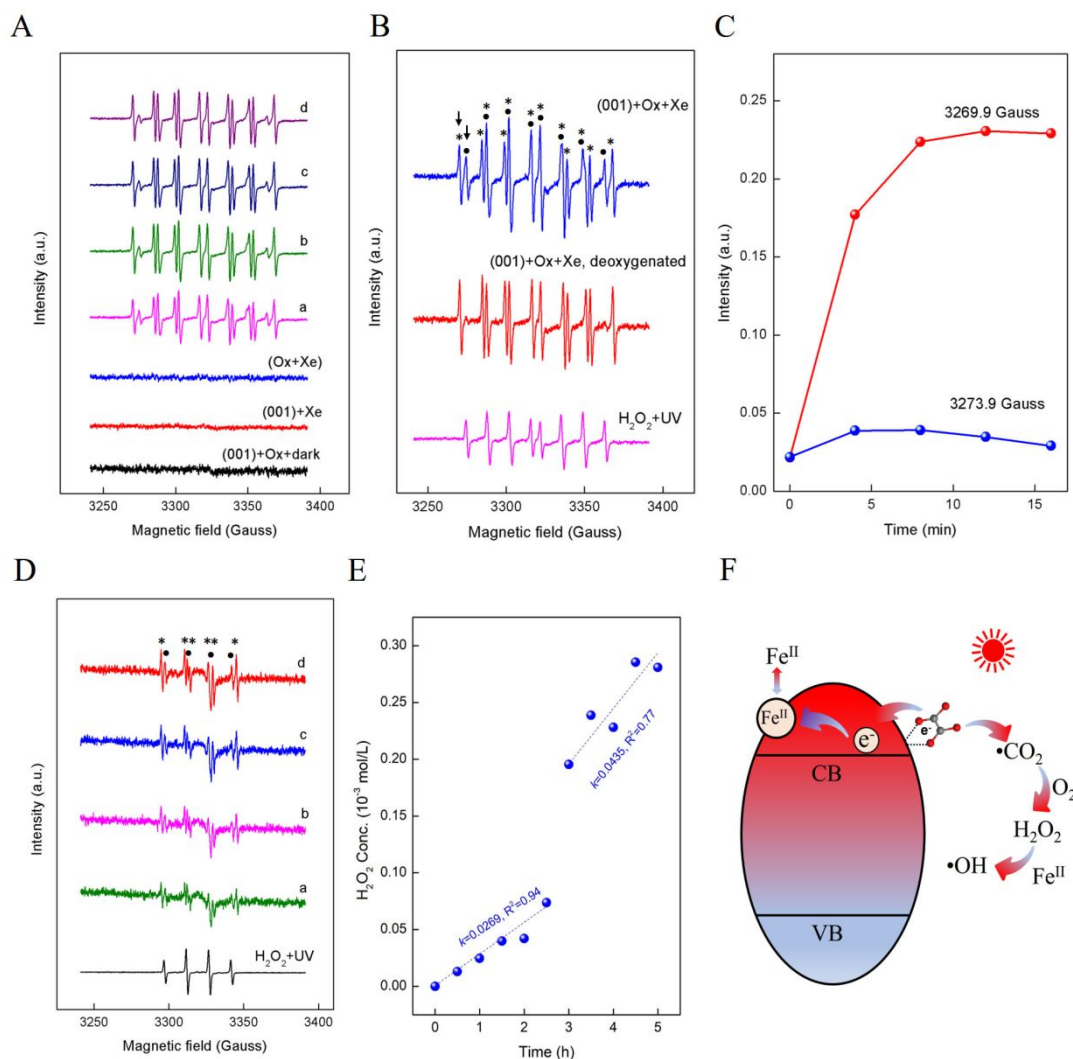
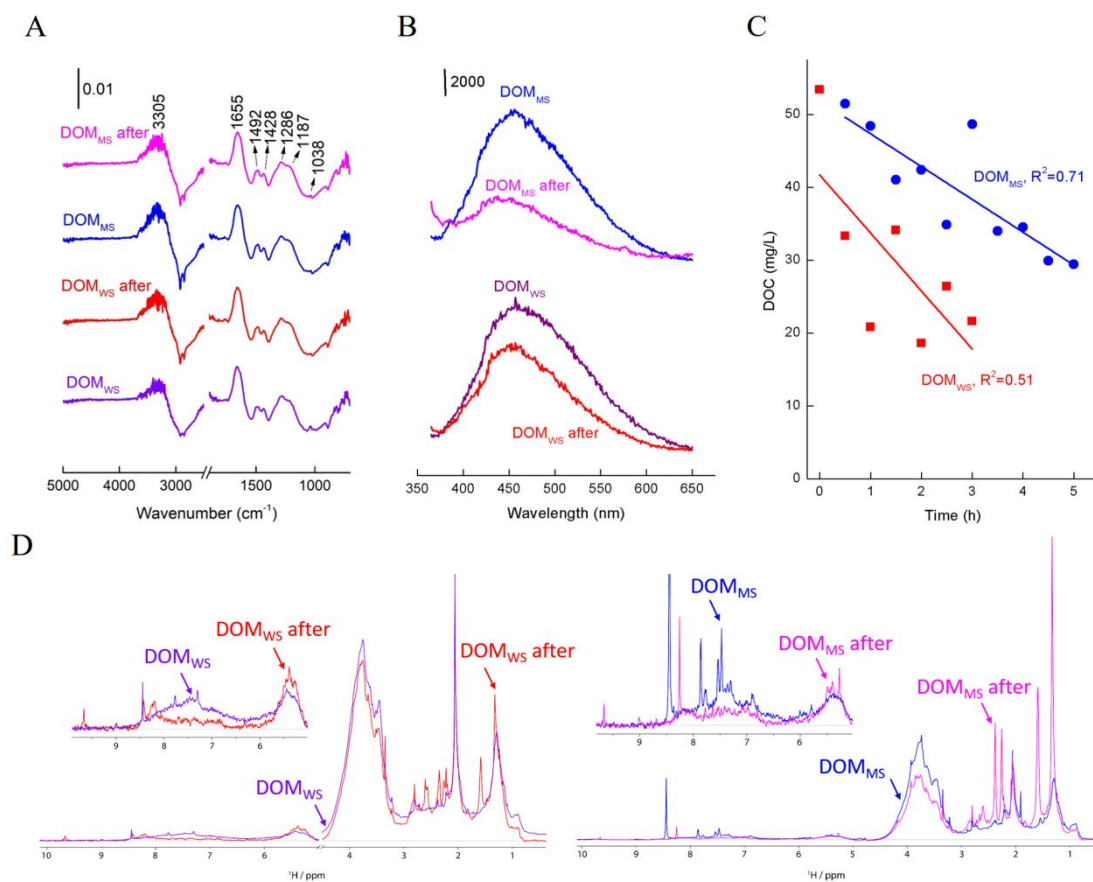


Figure 4. EPR spectroscopy to measure the generation of the radicals. (A) DEPMPO-trapped EPR signal changes in aqueous solutions as a function of time with hematite and oxalate ions under illumination (a, b, c, and d represent 4, 8, 12, and 16 min, respectively). (B) Peaks labeling in DEPMPO-trapped EPR spectra. The peaks that correspond to hydroxyl radicals and carboxyl anion radicals are labeled as “•” and “*”, respectively. (C) The intensity of the corresponding radicals in DEPMPO-trapped EPR spectra changes as a function of reaction time. (D) DMPO-trapped EPR signal changes in aqueous solutions as a function of time with hematite and oxalate under illumination. (E) The generation of hydrogen peroxide as reaction time. k and R^2 were pseudo-zero-order-rate constants of photoproduction of hydrogen peroxide in the solution and the corresponding fitting correlation coefficient values, respectively. (F) Conceptual schematic

1 representation of iron photochemical cycling coupling with reactive oxygen species generation that
2
3 are mediated by oxalate under sunlight illumination.
4

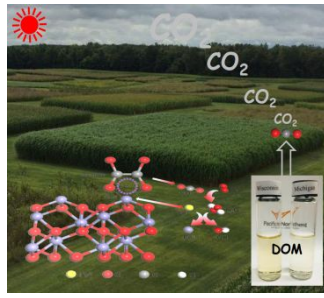


5
6
7
8
9
10
11
12
13
14
15
16
17
18
19
20
21
22
23
24
25
26
27
28
29
30
31
32
33
34
35 **Figure 5.** Photodegradation of chromophoric dissolved organic matter (DOM) in the presence of
36 hematite and oxalate. (A) ATR-FTIR spectra of the DOM before and after the photoreaction. (B)
37 Fluorescence spectra of the DOM before and after the photoreaction. (C) Photodegradation kinetics
38 of DOM in the presence of hematite and oxalate under illumination. (D) 1D ¹H NMR spectra of
39 DOM_{WS} (left) and DOM_{MS} (right) before and after photodegradation with magnified expansion of
40 the aromatic and olefinic regions (5.3 – 10.0 ppm). For the stacked display, the DOM_{WS} “after”
41 spectrum intensity was multiplied by a factor of 1.29 to make its total integrated area equal to the
42 “before” spectrum. No such scaling was required for DOM_{MS}.
43
44
45
46
47
48
49
50
51
52
53
54
55
56
57
58
59
60

Table 1. Results of the regional binning and integration of the 1D ^1H NMR spectra of DOM_{WS} and DOM_{MS} acquired before (dark control) and after exposure to light in the presence of hematite nanoparticles and oxalate. The predominant substructures and chemical shift ranges for the regions used are on the left side of the table. The percent (%) integrated (int.) area (A) is the contribution of each region to the total integrated area in each spectrum. The percent change was calculated as (% int. A_{after} - % int. A_{before})/(% int. A_{before}).

Type	$\delta(^1\text{H})$ region (ppm)	DOM_{WS}			DOM_{MS}		
		% int. A before	% int. A after	% Change	% int. A before	% int. A after	% Change
$\text{HC}_{\text{aromatic}}$	10.0 - 7.0	4	2	-48	5	2	-56
$\text{HC}=\text{C}/\text{O}_2\text{CH}$	7.0 - 5.3	4	3	-13	3	2	-23
OCH	4.5 - 3.1	55	51	-8	52	35	-32
XCCH	3.1 - 1.9	20	24	22	20	28	39
CCCH	1.9 - 0.5	18	20	12	20	33	61

Table of contents entry



- 1
- 2
- 3
- 4
- 5
- 6
- 7
- 8
- 9
- 10
- 11
- 12
- 13
- 14
- 15
- 16
- 17
- 18
- 19
- 20
- 21
- 22
- 23
- 24
- 25
- 26
- 27
- 28
- 29
- 30
- 31
- 32
- 33
- 34
- 35
- 36
- 37
- 38
- 39
- 40
- 41
- 42
- 43
- 44
- 45
- 46
- 47
- 48
- 49
- 50
- 51
- 52
- 53
- 54
- 55
- 56
- 57
- 58
- 59
- 60